Journal of Advanced Ceramics
2020, **9**(4): 432–443
https://doi.org/10.1007/s40145-020-0386-5

ISSN 2226-4108
CN 10-1154/TQ

Research Article

Microstructure and luminescent properties of Eu^{3+}-activated $MgGa_2O_4:Mn^{2+}$ ceramic phosphors

A. LUCHECHKO[a], Y. SHPOTYUK[a,b], O. KRAVETS[a], O. ZAREMBA[c], K. SZMUC[b], J. CEBULSKI[b], A. INGRAM[d], R. GOLOVCHAK[e], O. SHPOTYUK[f,g,*]

[a]*Department of Sensor and Semiconductor Electronics, Ivan Franko National University of Lviv, Lviv 79017, Ukraine*
[b]*Institute of Physics, University of Rzeszow, Rzeszow 35959, Poland*
[c]*Department of Inorganic Chemistry, Ivan Franko National University of Lviv, Lviv 79005, Ukraine*
[d]*Opole University of Technology, Opole 45370, Poland*
[e]*Department of Physics, Engineering and Astronomy, Austin Peay State University, Clarksville, TN 37044, USA*
[f]*Faculty of Science and Technology, Jan Dlugosz University, Czestochowa 42200, Poland*
[g]*Vlokh Institute of Physical Optics, Lviv 79005, Ukraine*

Received: February 27, 2020; Revised: May 12, 2020; Accepted: May 18, 2020

Abstract: Mn^{2+} and the trivalent europium (Eu^{3+})-doped $MgGa_2O_4$ ceramics are characterized using a multi-experimental approach. The formation of spinel-structured ceramics is ascertained from X-ray diffraction (XRD) analysis. Morphology investigations with transmission electron microscopy (TEM) show irregularly shaped grains and grain boundaries with a homogeneous distribution of Eu^{3+} ions. The inability of Eu activator to penetrate the bulk of ceramic grains is inferred from positron annihilation lifetime spectroscopy data. The Eu doping is shown to enhance the positron trapping rate due to the occupancy of vacancy-type defects at ceramic grains by Eu^{3+} ions. Both Mn^{2+} and Eu^{3+} doped samples show a broad multi-color luminescence in 350–650 nm range under 240 nm and 270–300 nm excitations. Blue emission is concluded to originate from host defects, whereas green emission and narrow lines in the red region of the spectrum are attributed to Mn^{2+} and Eu^{3+} ions, respectively. High asymmetry around Eu^{3+} ions can be concluded from the photoluminescence and positron annihilation lifetime spectra analysis.

Keywords: spinel structure; magnesium gallate $MgGa_2O_4$; X-ray diffraction (XRD); positron annihilation; Mn^{2+} and Eu^{3+} luminescence

1 Introduction

Flat-panel displays (plasma, field-emission, electro-luminescence, etc.) have drawn much interest recently due to their ultimate importance for modern electronics. The spinel oxide compounds are shown to be very appealing candidates for such applications due to their superior optical transparency, high thermal, and chemical stability, as well as electronic and magnetic properties [1–4]. As a result, the luminescent spinel-structured phosphors have emerged as one of the key materials

* Corresponding author.
E-mail: olehshpotyuk@yahoo.com

comprising an archetypal research challenge in nowadays optoelectronics [1–5]. For a long period, the 380 nm pumping radiation obtained from conventional ZnO electroluminescence or ultraviolet light-emitting diode (UV-LED) technology was used for the excitation of phosphors in flat-panel display systems. Recent optimization of micropillar approaches has boosted the deep UV-LED (DUV-LED) technologies, which enabled a new class of materials to be used in flat-panel display applications. The novel DUV-LEDs usually provide a quite powerful pumping (~150 mW) in UV spectral range with a maximum at 265 nm [6]. Currently, DUV-LED technology is on the way to be improved in terms of stability and power consumption [6].

The trivalent europium (Eu^{3+}) plays an important role as photoluminescent (PL) ion in phosphors due to its narrow emission bands in the orange region [5,7]. The PL of $MgGa_2O_4$ ceramics doped with Eu^{3+} has been studied in Refs. [1,8,9], while those activated by Mn^{2+} dopants were analyzed in Refs. [2,3,10–13]. It was shown that PL properties of such phosphors are strongly dependent on calcination temperature during synthesis procedure [1,3], affecting both the grain size [1] and the concentration of doping ions [2,8,10,11,13]. The combination of orange PL associated with Eu^{3+} dopants with blue intrinsic PL of host lattice and green PL of Mn^{2+} ions makes it possible to obtain phosphors in the visible range of spectrum using spinel-type compounds alone [8,9]. Despite a vast interest in the magnesium gallate spinels (including $MgGa_2O_4$) in view of their possible applications, the PL mechanisms of Eu^{3+} ions and their incorporation into spinel host matrix is still a matter of hot debates. To our best knowledge, the correlation between PL and structure of spinel gallates has not been studied. There are only a few papers concerning the relationship between defect structure and PL in zinc gallate ($ZnGa_2O_4$) spinel [14,15], while similar studies for $MgGa_2O_4$ spinel have not been reported yet.

In this study, spinel-structured non-transparent $MgGa_2O_4$ ceramic phosphors prepared by solid-state reactions and doped with Mn^{2+} and Eu^{3+} activators are comprehensively characterized with X-ray diffraction (XRD), scanning transmission electron microscopy (STEM) with energy-dispersive X-ray spectroscopy (EDS) analysis, positron annihilation lifetime (PAL) spectroscopy, and photoluminescent (PL) methods. The use of a multi-experimental approach allowed us to shed more light on the correlation between PL mechanism and preferential surroundings of Eu^{3+} activators in these ceramic phosphors.

2 Experimental

2. 1 Sample preparation

The $MgGa_2O_4$: 0.05 mol% Mn^{2+} and $MgGa_2O_4$: 0.05 mol% Mn^{2+}, 4 mol% Eu^{3+} ceramics were prepared using standard high-temperature ceramic technology. The host material was prepared from simple oxides of magnesium and gallium (MgO, β-Ga_2O_3). The doping was implemented by substitution of magnesium and gallium oxides with manganese (Ⅱ) oxide (MnO) and europium (Ⅲ) oxide (Eu_2O_3) of the same molar amount. The optimal concentration of Mn^{2+} and Eu^{3+} activator ions was chosen to have a maximum yield of luminescence in green and orange-red spectral regions, respectively. The initial powders were at least of 4N purity. The mixing of the powders was carried out in agate mortar for 6 h with further pressing in a steel mold. The obtained pellets were heated with 5 ℃/min ramp up to 1200 ℃ (±5 ℃), held at this temperature for 8 h and cooled down to room temperature in the regime of the switched-off furnace.

2. 2 Microstructure characterization

The structure of prepared ceramics was studied with XRD analysis. Experimental XRD patterns were collected using the STOE STADI P diffractometer equipped with a linear position-sensitive detector and X-ray tube with Cu anode ($K\alpha_1$-radiation, λ = 1.5406 Å). The measurements were carried out with 0.005° scanning step and the diffraction peaks were analyzed with the STOE WinXPOW software package.

Morphology of intrinsic grains in the ceramics was investigated using the TEM method complemented by EDS analysis (FEI Tecnai Osiris device). The atomically resolved information was obtained through a combination with a high-angle annular dark-field (HAADF) detector. The investigated samples were powdered with agate mortar and pestle, suspended in ethanol, sonicated for 5 min, placed onto the TEM Cu grid, and dried at the ambient temperature.

The free-volume structure on the atomic scale was studied with PAL spectra analysis. These spectra were recorded using a fast-fast coincidence system of 230 ps

resolution (full width at half maximum) equipped with two Photonis XP2020/Q photomultiplier tubes coupled to BaF_2 scintillator detectors. The ^{22}Na isotope (~50 kBq) sealed in Kapton film was used as a positron source, which was sandwiched between 2 identical samples. The experiments were performed in controlled conditions (22 ℃ ambient temperature and 35% humidity) collecting the normal statistics of 1M annihilation events. Three measurements for each sample were performed to ensure reproducibility of the results. The software LT 9.0 program [16] was used to decompose the raw PAL spectra into three exponentials, which contain information about the annihilation of positrons within defect-free bulk, trapped in free-volume defects, and forming bound positron-electron states (positronium Ps). The resultant accuracy in lifetime (τ_i) and intensity (I_i) was ±0.005 ns and ±0.5%, respectively. The positron trapping was parameterized by mean positron lifetime (τ_{av}), defect-free bulk lifetime (τ_b), trapping rate in defects (κ_d), and fraction of trapped positrons (η) defined within two-state simple trapping model (STM) [17–19], applied in addition to Ps-decay contribution [20]. Following the interpretation of free-volume positron trapping [17], the difference between defect-specific and defect-free lifetime ($\tau_2 - \tau_b$) was accepted as a signature of positron traps in terms of the equivalent number of vacancies, whereas τ_2/τ_b ratio was ascribed to the nature of these defects.

2. 3 Optical-PL characterization

Optical absorption spectra of the ceramics in 200–800 nm range were recorded at room temperature using a double-beam spectrophotometer Agilent Cary 5000. The optical absorption setup was equipped with Agilent diffuse reflectance accessory focusing an integrated signal to the detector.

PL characterization of the studied ceramics was carried out at room temperature employing SM 2203 spectrofluorometer operated in 230–820 nm range. The PL excitation was performed with a 150 W Xenon lamp, the Hamamatsu R928 photomultiplier being used for spectra detection. Both PL excitation and emission spectra were registered with a resolution of 0.5 nm and automatically corrected by lamp intensity and photomultiplier tube sensitivity. Additional PL measurements at room (T_R = 298 K) and liquid nitrogen (T_{LN} = 77 K) temperatures were performed for Eu^{3+} doped $MgGa_2O_4$:Mn^{2+} ceramics using Horiba Fluorolog-3 spectrofluorometer equipped with Xenon short-arc lamp as a light source. The PL emission spectra were collected in 300–640 nm range with excitation wavelength in 235–585 nm range.

3 Results and discussion

3. 1 Phase composition and atomic-specific structure

The Rietveld refinement analysis of ceramic samples with nominal compositions of $MgGa_2O_4$: 0.05 mol% Mn^{2+} and $MgGa_2O_4$: 0.05 mol% Mn^{2+}, 4 mol% Eu^{3+} was carried out for XRD patterns shown in Fig. 1. Besides the main $MgGa_2O_4$ phase ($MgAl_2O_4$ structure type, Pearson symbol *cF*56, space group *Fd*-3*m* (227)), a negligible amount of Ga_2O_3 phase (Pearson symbol *mS*20, space group *C*2/*m*(12)) was found in $MgGa_2O_4$:Mn^{2+} ceramics (Table 1). In Eu-doped $MgGa_2O_4$:Mn^{2+} samples, about 2.3 mol% of additional $Eu_3Ga_5O_{12}$ phase ($Y_3Al_5O_{12}$ structure type, Pearson symbol *cI*160, space group *Ia*-3*d* (230)) was revealed to coexist with the main $MgGa_2O_4$ spinel phase (Table 2).

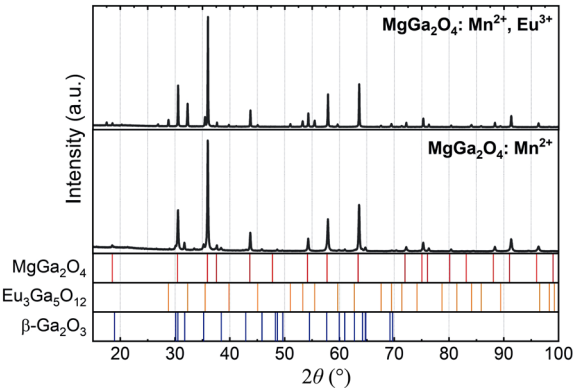

Fig. 1 Experimental XRD patterns of $MgGa_2O_4$:Mn^{2+} and $MgGa_2O_4$:Mn^{2+},Eu^{3+} ceramics (the theoretical Bragg reflections of corresponding phases are shown for comparison at the bottom).

Table 1 Atomic coordinates of spinel phase in $MgGa_2O_4$:Mn^{2+} ceramics (cell parameter, a = 8.2704(1) Å, R-factor = 2.44)

Site	Wyckoff position	Atomic coordinates			Occupancy
		x	*y*	*z*	
O	32*e*	0.2441	0.2441	0.2441	1
Mg1	16*c*	0	0	0	0.46(1)
Ga1	16*c*	0	0	0	0.54(1)
Mg2	8*b*	3/8	3/8	3/8	0.18(1)
Ga2	8*b*	3/8	3/8	3/8	0.82(1)

Table 2 Atomic coordinates of spinel phase in Eu-doped $MgGa_2O_4$:Mn^{2+},Eu^{3+} ceramics (a = 8.2726(1) Å, R-factor = 3.17)

Site	Wyckoff position	Atomic coordinates			Occupancy
		x	*y*	*z*	
O	32*e*	0.2441	0.2441	0.2441	1
Mg1	16*c*	0	0	0	0.48(1)
Ga1	16*c*	0	0	0	0.52(1)
Mg2	8*b*	3/8	3/8	3/8	0.17(1)
Ga2	8*b*	3/8	3/8	3/8	0.83(1)

Similar content of additional garnet phase was also observed in Eu-doped $ZnGa_2O_4$:Mn^{2+} ceramics recently [14]. Zhang *et al*. [15] used a facile hydrothermal method to synthesize $ZnGa_2O_4$ ceramics doped with a small amount (< 5 mol%) of Mn^{2+} or Eu^{3+} ions, but no additional phase was detected. Li *et al*. [21] reported the $Eu_3Ga_5O_{12}$ phase in Eu-doped $MgGa_2O_4$ ceramics at the concentration of Eu^{3+} ions above 5 mol%, whereas Sawada *et al*. [22] observed no Eu^{3+} emission for $Eu_3Ga_5O_{12}$ garnet. Owing to low concentration in our samples, it looks like the additional garnet phase does not affect the properties of the investigated $MgGa_2O_4$ ceramics, and would not be discussed further.

The refined structural data show that both $MgGa_2O_4$:Mn^{2+} and Eu-doped $MgGa_2O_4$:Mn^{2+} ceramics possess a partially inversed spinel structure. However, a normal spinel structure without inversion has been reported recently for similar ceramics obtained with this technology and with identical concentrations of Mn and Eu dopants [14]. This apparent controversy is due to a high number of singly charged point defects $[Ga_{tetrh}]^{+}$ and $[Mg_{octh}]^{-}$ caused by cation exchange between tetrahedral and octahedral sites, which is the reason for inverse spinel structure of the investigated magnesium gallate compounds, as well as changes in their physical properties.

Embedding the Eu^{3+} ions into a spinel-structured $MgGa_2O_4$ host matrix leads to a small increase in cell parameters, whereas the rest of unsolvable europium oxide Eu_2O_3 forms an additional garnet phase. Additional process in the structure of Eu-doped $MgGa_2O_4$:Mn^{2+} ceramics can be suspected because of much higher R-factor concerning that observed in $MgGa_2O_4$:Mn^{2+} ceramics.

3. 2 Grain morphology

The HAADF−STEM images of both $MgGa_2O_4$:Mn^{2+} and Eu-doped $MgGa_2O_4$:Mn^{2+} spinel-structured ceramics are shown in Figs. 2(a) and 2(b), respectively. The observed grains of irregular shape seem to be a common feature of these ceramics prepared by solid-state synthesis [14,21].

The EDS maps of $MgGa_2O_4$:Mn^{2+} and $MgGa_2O_4$:Mn^{2+},Eu^{3+} ceramics are presented in Figs. 2(a), 2(c), 2(e), and 2(g), and Figs. 2(b), 2(d), 2(f), 2(h), and 2(i), respectively. Homogeneous distribution of Eu across grain surfaces is evident from the EDS map for Eu-doped ceramics (Fig. 2(i)). At the same time, the concentration of Mn^{2+} dopant is too low to be detected unambiguously by this technique.

The electron diffraction patterns of both $MgGa_2O_4$:Mn^{2+} and $MgGa_2O_4$:Mn^{2+},Eu^{3+} ceramics are shown in Figs. 3(a) and 3(b). Figure 3 demonstrates typical patterns of polycrystalline material with sharp reflexes from 400, 422, 440, 533, and 731 planes of spinel phase and no traces of other additional phases.

3. 3 Nanovoid structure

Based on the PAL spectroscopy data, it can be concluded that Eu^{3+} ions do not penetrate deeply into the grains of spinel-structured $MgGa_2O_4$:Mn^{2+} ceramics.

The raw PAL spectra of these ceramics are presented in Fig. 4, while corresponding parameters of the unconstrained three-exponential fits are gathered in Table 3. The results show only a slight growing tendency in τ_{av} of the Eu-doped ceramics (Fig. 5 compares PAL spectra of both ceramics).

In the developed approach to spinel-type ceramics [23], the second component (τ_2, I_2) in the decomposed PAL spectrum can be attributed to a positron trapping in vacancies and vacancy-like free-volume defects located preferentially near grain boundaries. The third long-lived lifetime component (τ_3, I_3) is responsible for Ps-decay through the "pick-off" annihilation of a positron with an electron from surrounding [17,20]. In spinel-structured ceramics, the Ps is known to be localized in free-volume holes within intergranular space [23], which means that radius R_3 of these holes can be calculated using τ_3 in the Tao–Eldrup approach [17]. Respectively, the intensity (I_3) correlates with the number of Ps sites, so that the fractional free volume (f_{v3}) can be calculated in a spherical approximation with some empirical constant [20].

Since only low contribution in the PAL spectra shown in Fig. 4 arises from the third component (the corresponding intensity I_3 in Table 3 does not exceed

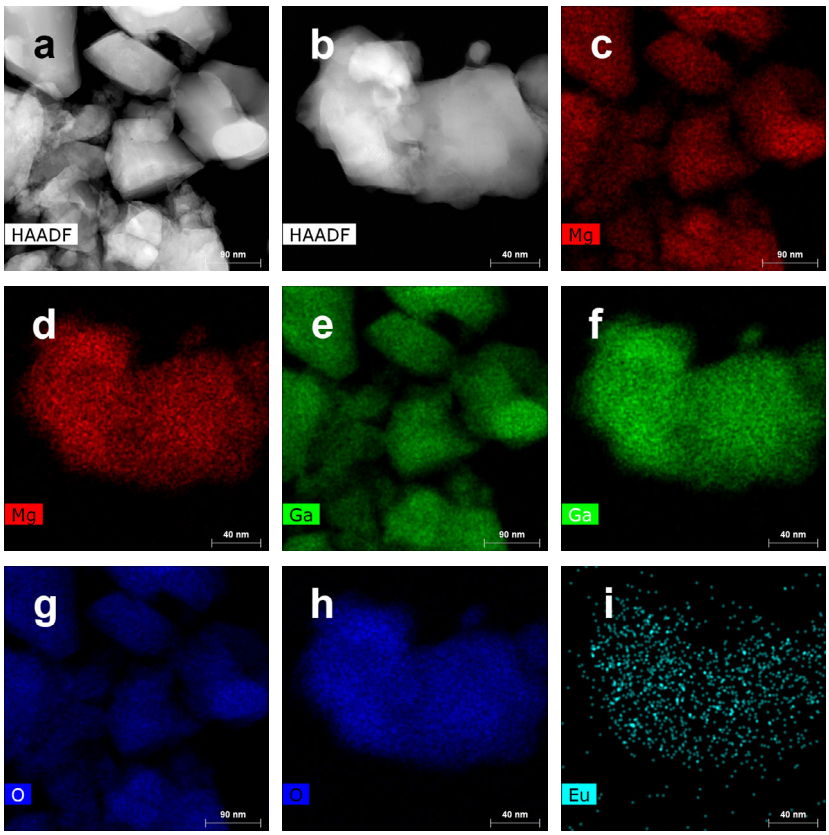

Fig. 2 HAADF–STEM images of (a) $MgGa_2O_4$:Mn^{2+} and (b) $MgGa_2O_4$:Mn^{2+},Eu^{3+} grains, with corresponding chemical composition EDS maps of (c, e, g) $MgGa_2O_4$:Mn^{2+} and (d, f, h, i) $MgGa_2O_4$:Mn^{2+},Eu^{3+} grains, representing location of each element in the grain.

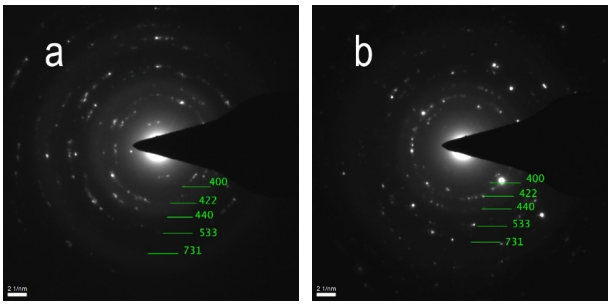

Fig. 3 Electron diffraction patterns of (a) $MgGa_2O_4$:Mn^{2+} and (b) Eu-doped $MgGa_2O_4$:Mn^{2+},Eu^{3+} ceramics.

0.013 a.u.), the realistic annihilation scheme in this ceramics can be quite adequately described within two-state STM [17–19], thus ignoring Ps-decay contribution [20]. The results of such parameterization are gathered in Table 4. This simplification allows us to conclude that Eu^{3+} doping enhances positron trapping in the studied $MgGa_2O_4$:Mn^{2+} ceramics (due to increased κ_d from 0.50 to 0.72 ns^{-1}). Realistically, this enhancement is counterbalanced by a decrease in f_{v3} calculated from Ps-related components. The high values of $(\tau_2 - \tau_b)$ reaching ~0.13–0.15 ns and

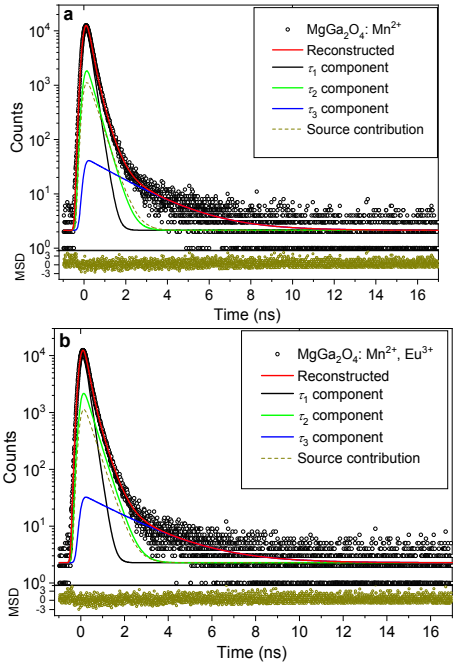

Fig. 4 Raw PAL spectra of spinel-structured (a) $MgGa_2O_4$:Mn^{2+} and (b) $MgGa_2O_4$:Mn^{2+},Eu^{3+} ceramics, reconstructed from unconstrained x3-term fitting and source contribution (bottom insets show statistical scatter of variance).

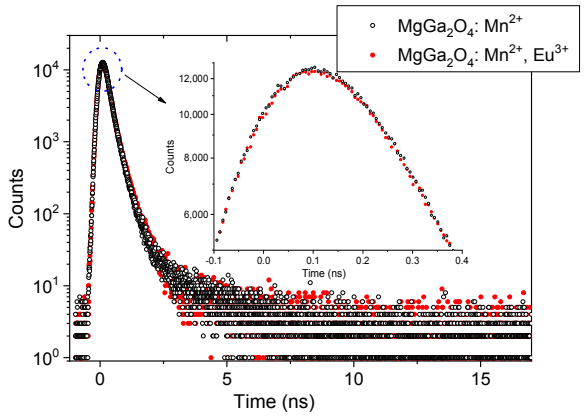

Fig. 5 Comparison of raw PAL spectra of spinel-structured $MgGa_2O_4$:Mn^{2+} and Eu-doped $MgGa_2O_4$:Mn^{2+} ceramics (the insert shows magnified peak region).

Table 3 PAL spectra fitting parameters for studied spinel-structured ceramics within unconstrained x3-term decomposition

Ceramics	Fitting parameter					τ_{av}(ns)
	τ_1 (ns)	τ_2 (ns)	τ_3 (ns)	I_2 (a.u.)	I_3 (a.u.)	
$MgGa_2O_4$:Mn^{2+}	0.172	0.322	2.142	0.180	0.013	0.224
$MgGa_2O_4$:Mn^{2+},Eu^{3+}	0.166	0.339	2.162	0.230	0.011	0.227

Table 4 PAL trapping modes for studied spinel-structured ceramics within unconstrained x3-term decomposition ignoring contributions from o-Ps decay

Ceramics	Positron-trapping mode					Ps-decay modes	
	τ_{av}^{tr} (ns)	τ_b (ns)	κ_d (ns^{-1})	$\tau_2-\tau_b$ (ns)	τ_2/τ_b (a.u.)	R_3 (nm)	f_{v3} (%)
$MgGa_2O_4$:Mn^{2+}	0.199	0.188	0.50	0.134	1.71	0.301	0.26
$MgGa_2O_4$:Mn^{2+},Eu^{3+}	0.206	0.188	0.72	0.151	1.80	0.302	0.22

τ_2/τ_b = ~1.7–1.8 (Table 4) suggest multivacancy clusters with free volumes comparable to triple or even quadruple vacancies [17,23] as prototypes of positron traps in both types of the studied ceramics. The role of Ps-decay input is somewhat depressed in Eu^{3+}-doped ceramics due to decreased probability of Ps formation, as it follows from opposite trends in I_3 and I_1 compared to I_2 [24].

In the case of well-separated inputs from positron trapping and Ps-decay contributions into the resulting PAL spectra, the Ps-positron trapping conversion can be analyzed with x3-x2-CDA (coupling decomposition algorithm) [25,26]. A similar approach was successfully used recently to analyze the reverse positron-to-Ps trapping interplay in zinc gallate ceramics [14]. Within this formalism, the unconstrained x3-term reconstructed PAL spectra are transformed into generalized x2-term form for both non-modified ($MgGa_2O_4$:Mn^{2+}) and modified (Eu-doped $MgGa_2O_4$:Mn^{2+}) ceramics assuming all possible trapping contributions (including ortho-Ps decay and para-Ps self-annihilation). This allows to resolve additional component in the generalized x2-term PAL spectrum for modified matrix (with defect-related positron lifetime (τ_{int}) and intensity (I_{int})) and compensating (τ_n, I_n) input to the first channel. The τ_{int} in this model reflects appeared/disappeared defect-related traps depending on the positive/negative sign of both I_n and I_{int} [14,25,26].

The comparison of trapping parameters calculated with the x3-x2-CDA for studied samples of spinel-structured ceramics is given in Table 5. Taking into account positive values of I_n and I_{int} intensities, the overall free-volume evolution caused by Eu^{3+} doping can be described as the replacement of Ps-decaying holes with τ_3 = 2.142 ns (corresponding to spheres of approximately ~0.30 nm in radius) by positron trapping free-volume defect with τ_{int} = 0.372 ns (the equivalent of multi-vacancy clusters [17,23]). Owing to close values of bulk positron lifetime for modified ceramics ($\tau_b^m \approx$ 0.18 ns) and defect-free bulk positron lifetime for spinel-structured compounds [26], we believe that respective positron traps (which should be quite extended due to large τ_{int}/τ_b^m ratio approaching ~2.1) are located deeply in ceramic grains. Therefore, the holes associated with Ps decay should stabilize predominantly at the ceramic grain boundaries.

The obtained results suggest that relative input of positron traps in an overall annihilation process in Eu-doped $MgGa_2O_4$:Mn^{2+} spinel-structured ceramics is enhanced as a result of Eu^{3+} ions localization in the Ps-decaying holes near ceramic grain boundaries. This should decrease their effective number, and consequently, depress the Ps-related component in the PAL spectra.

3.4 Optical absorption

The optical absorption spectra of both ceramics are shown in Fig. 6. The $MgGa_2O_4$:Mn^{2+} spinel-structured ceramics show an intense absorption band in the UV region of

Table 5 PAL trapping modes for $MgGa_2O_4$:Mn^{2+},Eu^{3+} ceramics defined in respect to $MgGa_2O_4$:Mn^{2+} ceramics within x3-x2-CDA

First component		Second component		Trapping modes			
τ_n (ns)	I_n (a.u.)	τ_{int} (ns)	I_{int} (a.u.)	τ_{av}^m (ns)	τ_b^m (ns)	κ_d^m (ns^{-1})	τ_{int}/τ_b^m (ns)
0.157	0.297	0.372	0.078	0.201	0.178	0.764	2.09

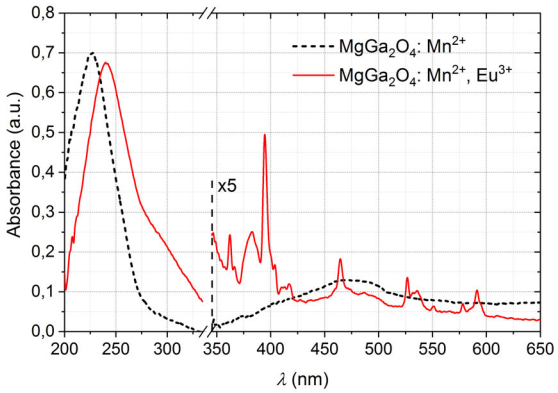

Fig. 6 Optical absorption spectra of spinel-structured $MgGa_2O_4$ ceramics activated with Mn^{2+} ions and co-doped with Mn^{2+} and Eu^{3+} ions (the long-wavelength part of the absorption signal is 5 times scaled).

the spectrum with a maximum around 240 nm (Fig. 6, black dashed line), which corresponds to "band-to-band" absorption in host $MgGa_2O_4$ matrix. The band gap energy estimated by extrapolation of the fundamental optical absorption edge for $MgGa_2O_4$:Mn^{2+} gives a value of about 4.8 eV. A broad absorption band is observed for $MgGa_2O_4$:Mn^{2+} ceramics in a 400–600 nm range with a maximum of around 480 nm. One of the possible origins of this broadband is Mn in the "4^+" state, which was observed earlier by Costa *et al.* [11]. However, we assume that Mn^{4+} ions have appeared in Ref. [11] due to a high sintering temperature of 1500 ℃ which caused strong evaporation of starting materials (primarily of gallium). The deficiency of host atoms led to the creation of vacancy defect and change in the valence state of a significant number of manganese ions. The conclusion on the substantial impact of sample preparation conditions on the manganese valence state is also supported by Moon *et al.* [2]. In our case, we have used lower sintering temperatures to avoid strong evaporation of initial precursors and obtained samples with minimal deviation from stoichiometry. We found no direct evidence on the existence of Mn^{4+} ions in the $MgGa_2O_4$:Mn^{2+} ceramics. Another explanation of a broad absorption band with a maximum at 480 nm is due to the resonant absorption in-between the levels formed by host defects. This explanation is supported by earlier results obtained on a series of $MgGa_2O_4$:Mn^{2+}, Eu^{3+} samples with various content of Eu^{3+} ions [8]. It was shown that Eu^{3+} ions substantially suppress the matrix emission, which correlates with the disappearance of the broad absorption band in the absorption spectrum of Eu-doped $MgGa_2O_4$:Mn^{2+} ceramics (Fig. 6, red solid line) and the results of PAL spectroscopy presented above.

The optical absorption spectrum of the Eu-doped $MgGa_2O_4$:Mn^{2+} ceramics demonstrates similar features (Fig. 6, red solid line), except that the maximum UV band is red-shifted due to the overlap with the intense band visible as shoulder around 290 nm. This shoulder is associated with charge transfer from 2p shell of oxygen anions to 4f shell of Eu^{3+} ions [9]. Sharp absorption lines observed on the right side of the absorption spectrum (Fig. 6) originate from f–f transitions in $4f^6$ configuration of Eu^{3+} ions. The most prominent line at 393 nm is identified as $^7F_0$–$^5L_6$ transition [1,9], while the rest of the lines observed at 414, 464, 525, and 583 nm are caused by $^7F_0$–^5D_j transitions with j value of 3, 2, 1, and 0, respectively. The energy-level diagram showing the observed absorption and emission are presented in Fig. 7.

3.5 Photoluminescence at room and liquid nitrogen (LN) temperatures

The PL properties of the $MgGa_2O_4$:Mn^{2+} and $MgGa_2O_4$:Mn^{2+},Eu^{3+} ceramics were studied at room temperature, and the results are presented in Figs. 8 and 9, respectively. The magnesium gallate ceramics doped with manganese ions show strong excitation in deep UV spectral region with a maximum at about 240 nm related to the fundamental absorption of magnesium gallate host under 505 nm monitoring wavelength (Fig. 6). This aspect indicates a favorable contribution of the recombination mechanism to manganese ion excitation [8,12]. Also, the existence of a strong green emission band of $MgGa_2O_4$:Mn^{2+} ceramics with a peak at 505 nm under the excitation of 240 nm UV light shows an efficient energy transfer from the host to the manganese activator ions. The

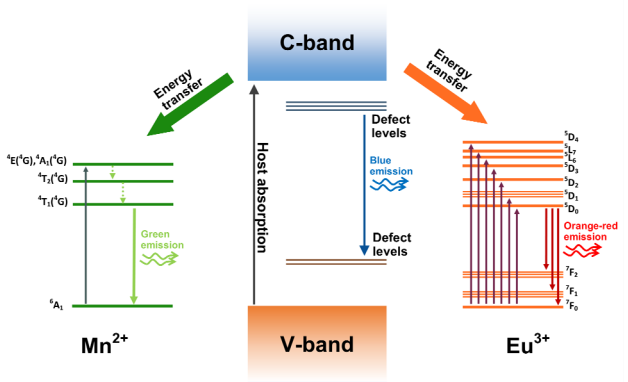

Fig. 7 Schematic energy-level diagram of Eu^{3+} and Mn^{2+} in $MgGa_2O_4$:Mn^{2+},Eu^{3+} ceramics.

shoulder at about 275 nm is assigned to charge transfer from oxygen to manganese ions. Another weak excitation found in the region of 325–450 nm is due to the matrix PL excitation [8] that partially overlaps with unresolved d–d excitation bands of Mn^{2+} ions [11–13]. The $MgGa_2O_4$:Mn^{2+} ceramics at 240 and 270 nm excitations show emission in two spectral regions of 320–470 nm and 470–550 nm related to host defects of the spinel structure and Mn^{2+} ions, respectively [2,8]. It should be noted that the relative intensity of the green emission associated with Mn^{2+} ions increases significantly with the excitation in the region of fundamental absorption edge, which is indirect evidence of the recombination mechanism. However, the relative intensity of PL from the matrix is comparable with activator PL at the excitation in the charge transfer band. According to Costa *et al*. [11] and Mironova *et al*. [27], luminescence at 505 nm is typical for divalent manganese cations in four-fold tetrahedrally coordinated sites corresponding to $^4T_1(^4G)\rightarrow{}^6A_1(^6S)$ transition in Mn^{2+}.

The PL excitation and emission spectra of Eu-doped $MgGa_2O_4$:Mn^{2+} ceramics monitored at 505 and 617 nm are shown in Fig. 9. These spectra occurred to be similar to those detected in $MgGa_2O_4$:Mn^{2+} samples (Fig. 8). However, the host and Mn^{2+} excitation bands in the range of 325–450 nm are effectively suppressed by the incorporation of Eu^{3+} emission. This effect is explained by the redistribution of the energy between Mn^{2+} and Eu^{3+} activators. Broad excitation band (charge transfer from O^{2-} to Eu^{3+} ions) and several excitation peaks in 350–550 nm region (f–f transition in Eu^{3+} ions), with two strongest ones at 393 ($^7F_0\rightarrow{}^5L_6$) and 462 ($^7F_0\rightarrow{}^5D_2$) nm were found under 617 nm monitored wavelength.

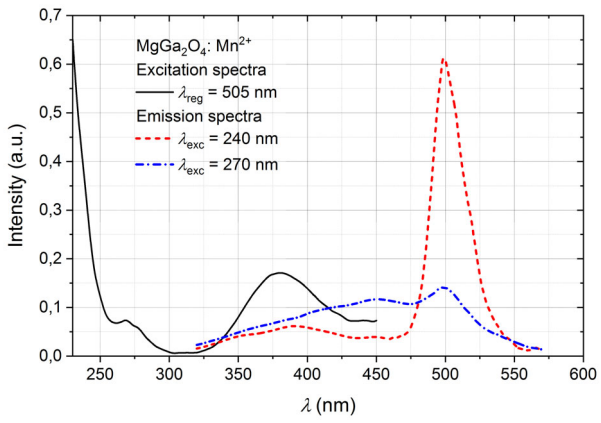

Fig. 8 PL excitation (black line) and emission spectra (red and blue lines) in $MgGa_2O_4$:Mn^{2+} ceramic sample.

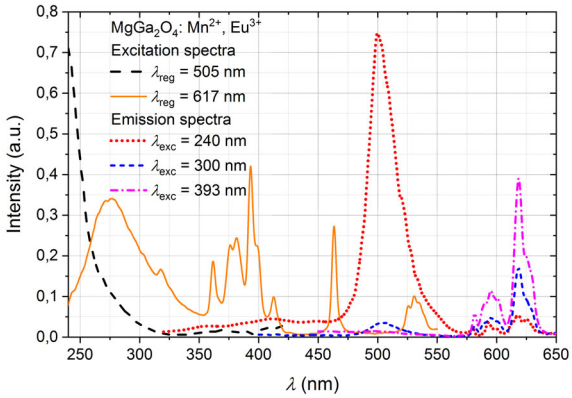

Fig. 9 PL excitation (black and red lines) and emission spectra (red, blue, and green lines) in $MgGa_2O_4$:Mn^{2+},Eu^{3+} ceramic sample.

In addition to the intense broadband PL centered at 505 nm associated with Mn^{2+} ions, the $MgGa_2O_4$:0.05Mn^{2+}, Eu^{3+} ceramics show emission at 575–650 nm, which belongs to the transitions from excited $^5D_0$ to ground ^7F_j (j=1, 2) level of the Eu^{3+} ions [1,8,9]. The strongest red emission at about 617 nm associated with $^5D_0\rightarrow{}^7F_2$ transition of Eu^{3+} ions is dominated in the PL spectrum. It should be noted that the matrix luminescence was completely suppressed in these ceramics after doping with Eu^{3+} ions.

It is well known that the local symmetry of Eu^{3+} sites in the lattice is reflected by a form of Eu^{3+} emission spectrum. According to the Judd–Ofelt theory [28,29], the magnetic dipole transition at about 593 nm ($^5D_0\rightarrow{}^7F_1$) is attributed to the ions with higher symmetry, while electric-dipole transitions at about 617 nm ($^5D_0\rightarrow{}^7F_2$) originate mainly from the ions in sites with lower symmetry. The more asymmetric is local surrounding around Eu^{3+} ion, the higher is the intensity of the electric-dipole transition (Fig. 9). The intense red emission of Eu^{3+} ions is caused by dominated electric-dipole transitions in Eu-doped $MgGa_2O_4$:Mn^{2+} spinel ceramics. Thus, the important parameter that has been used to identify site symmetry of Eu^{3+} ions is the intensity ratio between magnetic-dipole and electric-dipole transitions, emitting at about 595 and 617 nm, respectively. The calculated asymmetry ratio ($^5D_0\rightarrow{}^7F_2$)/($^5D_0\rightarrow{}^7F_1$) for $MgGa_2O_4$:Mn^{2+},Eu^{3+} ceramics is equal to 3.4 for the intensities (I_{617}/I_{593}), and 2.7 for the areas of respective group lines ($S_{605\text{-}640}/S_{585\text{-}605}$). The above-obtained asymmetry values suggest that coordination polyhedron around Eu^{3+} ions is rather distorted or asymmetric, i.e., the Eu^{3+} ions occupy non-inversion symmetry sites in a spinel lattice of

these ceramics.

The three dimentional (3D) fluorescence spectra of Eu^{3+} doped $MgGa_2O_4$:Mn^{2+} ceramics at room and LN temperatures are compared in Fig. 10. At LN temperature, the PL within 320–360 nm caused by the excitation at ~240 nm wavelength diminishes, while the PL within 370–440 nm region becomes more prominent (Figs. 10(a) and 10(b)). The PL intensity also increases at around 595 and 620 nm when excited with light of 468, 528, and 580 nm at LN temperature (T_{LN}) (Figs. 10(c) and 10(d)). At the same time, the intensity of PL at around 620 nm with excitation at ~350, ~375, and ~395 nm decreases compare to PL at room temperature (Figs. 10(c) and 10(d)).

The luminosity Commission Internationale de l'Éclairage (CIE) diagram of spinel-structured magnesium gallate ceramic samples is shown in Fig. 11. The solid blue curve represents the temperature emission of the black body. This curve is surrounded by A, B, C circles defining standard illuminants. The E corresponds to the point of achromatic white color, and D_{65} corresponds to the color of black body emission at 6500 K.

The respective emission colors of the prepared $MgGa_2O_4$ ceramics are marked by squares 1–5 (Fig. 11). The first point represents the emission of $MgGa_2O_4$:Mn^{2+} ceramics with 240 nm excitation and shows a bluish-green color due to the strong emission of Mn^{2+} ions and weak matrix PL. The same sample with 270 nm excitation exhibits greenish-blue PL (point 2) that is caused by the dominant broad emission band of the spinel matrix and addition of green Mn^{2+} PL emission. Taking into account the previously reported PL excitation spectra of completely "pure" magnesium gallate $MgGa_2O_4$ and manganese-modified $MgGa_2O_4$:Mn^{2+} spinel-structured ceramics [8], we conclude that both spectra are overlapped in the UV region. Thus, it is not possible to obtain only matrix or Mn^{2+} emission in the $MgGa_2O_4$:Mn^{2+} ceramics, since the first and second points, show edges of possible PL emission color in manganese-doped gallate spinel.

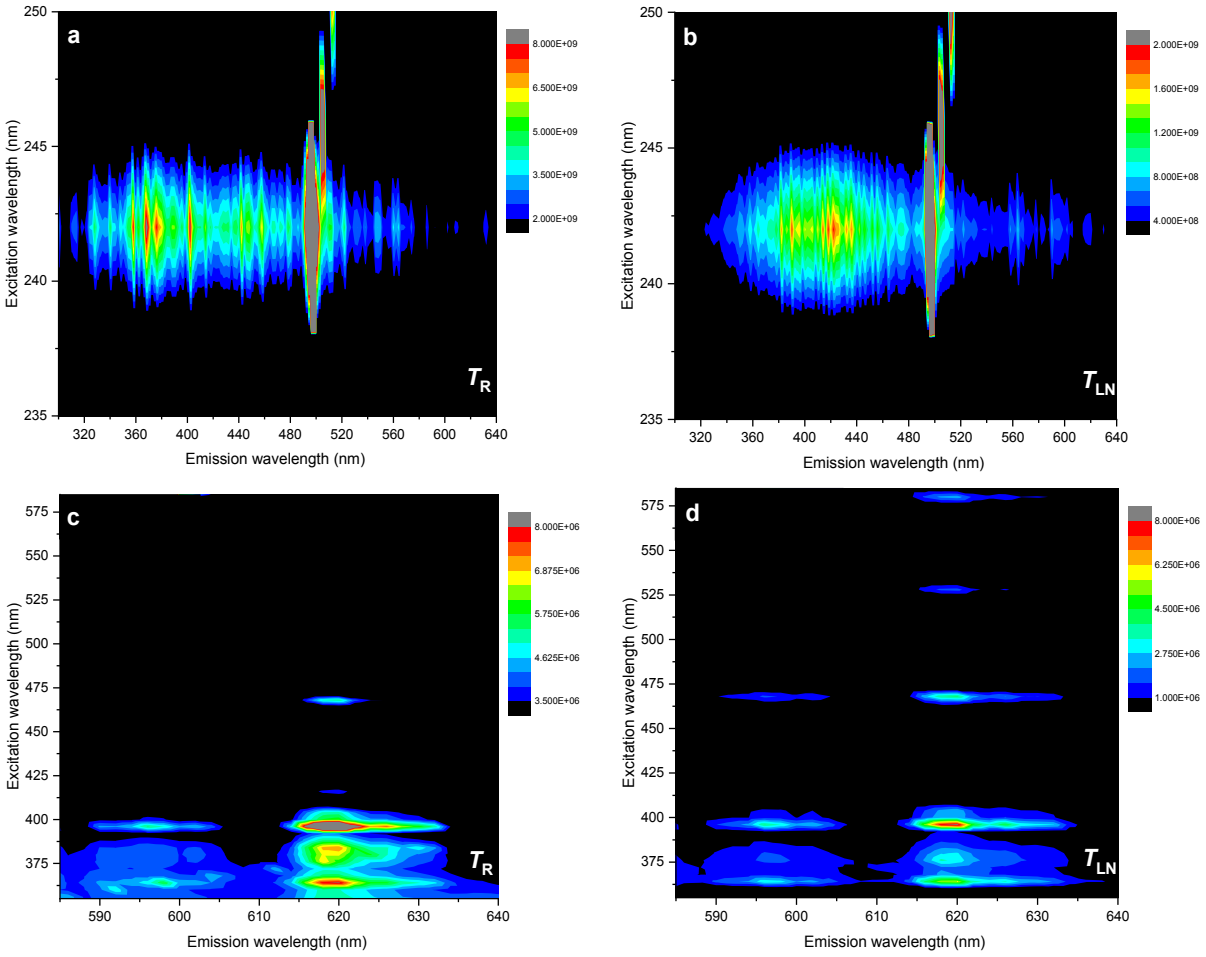

Fig. 10 PL spectra of Eu-doped $MgGa_2O_4$:Mn^{2+} ceramics recorded at (a, c) room temperature and (b, d) LN temperature.

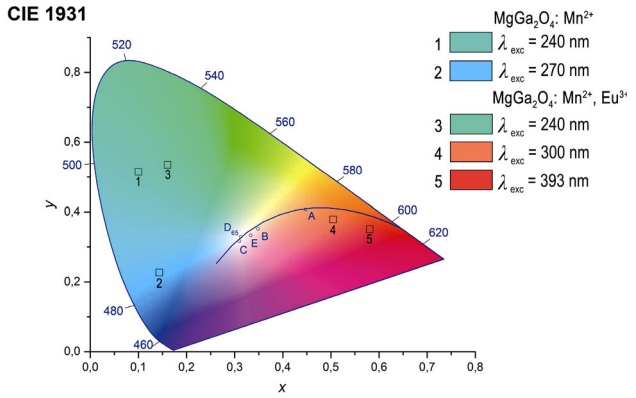

Fig. 11 CIE chromaticity diagram of the $MgGa_2O_4:Mn^{2+}$ and $MgGa_2O_4:Mn^{2+},Eu^{3+}$ ceramics with emission color samples at different excitations with respect to black body curve and A–E standard illuminants.

The emission colors of Eu-doped $MgGa_2O_4:Mn^{2+}$ spinel-structured ceramics are represented by the points 3–5 and corresponding squares 3–5 on Fig. 11. The PL emission of the Eu-doped sample with excitation at 240 nm is located close to point 1 but shifted a little bit towards the green region. The observed small shift is explained by the weakening of the host matrix PL concerning $MgGa_2O_4:Mn^{2+}$ sample that causes an increase in the green color PL emission. The applied 300 nm excitation leads to further weakening of the PL emission from Mn^{2+} ions and the matrix PL. Point 4 shows the reddish–orange color, which is related to the emission of Eu^{3+} ions in the "orange–red" spectral region. The excitation at f–f lines (393 nm) is presented by the emission of Eu^{3+} ions only, and shows a red color with little addition of the orange (point 5, Fig. 11). The calculated CIE achromatic coordinates under different light excitations for $MgGa_2O_4:Mn^{2+}$ and Eu-doped spinel-structured $MgGa_2O_4:Mn^{2+}$ ceramics are listed in Table 6.

In the studied $MgGa_2O_4:Mn^{2+},Eu^{3+}$ phosphors, the purity of the colors obtained at different excitation wavelengths ranges from 53% to 81%. The highest color purity is observed at the f–f intra-center excitation of Eu^{3+} ions (λ_{exc} = 393 nm, point 5 on the CIE diagram). It should be noted that most commercial phosphors activated by Eu^{3+} ions demonstrate a color purity of more than 90%. At the same time, in the case of $MgGa_2O_4$ spinel, there is a considerable inversion of the structure, and part of Eu^{3+} ions occupies inversion symmetry sites which can lead to a decrease in color purity.

Table 6 CIE achromatic coordinates calculated for both $MgGa_2O_4:Mn^{2+}$ and $MgGa_2O_4:Mn^{2+},Eu^{3+}$ ceramics under different excitations

Point number	Ceramics	Excitation wavelength (nm)	CIE coordinates	
			x	*y*
1	$MgGa_2O_4:Mn^{2+}$	240	0.10	0.51
2	$MgGa_2O_4:Mn^{2+}$	270	0.14	0.23
3	$MgGa_2O_4:Mn^{2+},Eu^{3+}$	240	0.16	0.54
4	$MgGa_2O_4:Mn^{2+},Eu^{3+}$	300	0.51	0.38
5	$MgGa_2O_4:Mn^{2+},Eu^{3+}$	393	0.58	0.35

4 Conclusions

The Rietveld refinement analysis of XRD patterns confirms the existence of the spinel phase in the structure of magnesium gallate $MgGa_2O_4:Mn^{2+}$ ceramics, whereas Eu-doped $MgGa_2O_4:Mn^{2+}$ ceramics show a small amount of $Eu_3Ga_5O_{12}$ phase. The homogeneous distribution of Eu dopants is proven by TEM–EDS mapping. The TEM morphology images show that ceramics grain sizes range from hundreds of nanometers to few micrometers. The inability of Eu activator to penetrate deeply into the $MgGa_2O_4$ ceramic grains is assumed from PAL spectroscopy results. The preferential location of Eu^{3+} ions in Ps-decay sites of the intergranular space leads to the enhanced positron trapping rate in Eu-doped $MgGa_2O_4:Mn^{2+}$ ceramics. Therefore, the overall structural evolution caused by Eu^{3+} doping in $MgGa_2O_4:Mn^{2+}$ ceramics can be described as the disappearance of Ps-trapping holes (0.30 nm in a radius) and formation of positron traps with defect lifetime equivalent of multi-vacancy clusters.

The $MgGa_2O_4:Mn^{2+}$ ceramics show intense green luminescence under 240 nm excitation, confirming the dominant contribution of the recombination mechanism. Selective excitation and excitation-dependent emission reveal few ways to excite the Eu^{3+} ions in $MgGa_2O_4:Mn^{2+}$ ceramics, all leading to the characteristic f–f emission in these ions. The Judd–Ofelt parameters calculated as the ratio between electric-dipole to magnetic-dipole transition shows that Eu^{3+} ions occupy sites of low symmetry within spinel $MgGa_2O_4$ lattice. The chromaticity coordinate values of $MgGa_2O_4:Mn^{2+}$ and Eu-doped $MgGa_2O_4:Mn^{2+}$ ceramics indicate that these phosphors can effectively emit different colors of light when excited with UV wavelength in 240–400 nm range.

Acknowledgements

This study is supported by the Ministry of Education and Science of Ukraine under the Young Scientists Program (0117U007189). R. GOLOVCHAK acknowledges the U.S. National Science Foundation (Grant No. DMR-1725188) for the acquisition of PAL spectrometer. J. CEBULSKI acknowledges support from the SAIA for partial support of this research within the National Scholarship Program of the Slovak Republic.

References

[1] Tsai BS, Chang YH, Chen YC. Nanostructured red-emitting $MgGa_2O_4:Eu^{3+}$ phosphors. *J Mater Res* 2004, **19**: 1504–1508.

[2] Moon YM, Choi S, Jung HK, *et al*. Sensitized photoluminescent properties of manganese-activated magnesium gallate phosphor. *J Lumin* 2008, **128**: 1491–1495.

[3] Choi S, Kim K, Moon YM, *et al.* Rapid synthesis of spherical-shaped green-emitting $MgGa_2O_4:Mn^{2+}$ phosphor via spray pyrolysis. *Mater Res Bull* 2010, **45**: 979–981.

[4] Tang YX, Zhang DF, Qiu XX, *et al.* Fabrication of a $NiCo_2O_4/Zn_{0.1}Cd_{0.9}S$ p-n heterojunction photocatalyst with improved separation of charge carriers for highly efficient visible light photocatalytic H_2 evolution. *J Alloys Compd* 2019, **809**: 151855.

[5] Gedekar KA, Wankhede SP, Moharil SV, *et al*. D–f luminescence of Ce^{3+} and Eu^{2+} ions in $BaAl_2O_4$, $SrAl_2O_4$ and $CaAl_2O_4$ phosphors. *J Adv Ceram* 2017, **6**: 341–350.

[6] Inoue SI, Tamari N, Taniguchi M. 150 mW deep-ultraviolet light-emitting diodes with large-area AlN nanophotonic light-extraction structure emitting at 265 nm. *Appl Phys Lett* 2017, **110**: 141106.

[7] Xia C, Yu CY, Cao MM, *et al*. A Eu and Tb co-doped MOF-5 compound for ratiometric high temperature sensing. *Ceram Int* 2018, **44**: 21040–21046.

[8] Luchechko A, Kravets O, Kostyk L, *et al*. Luminescence spectroscopy of Eu^{3+} and Mn^{2+} ions in $MgGa_2O_4$ spinel. *Radiat Meas* 2016, **90**: 47–50.

[9] Luchechko A, Kravets O. Novel visible phosphors based on $MgGa_2O_4$–$ZnGa_2O_4$ solid solutions with spinel structure co-doped with Mn^{2+} and Eu^{3+} ions. *J Lumin* 2017, **192**: 11–16.

[10] Osada M, Takesada M, Isobe T. Comparison between $MgGa_2O_4:Mn^{2+}$ and $ZnGa_2O_4:Mn^{2+}$ nanophosphors synthesized by glycothermal method. *ECS Transactions* 2009, **16**: 75–80.

[11] Costa GKB, Pedro SS, Carvalho ICS, *et al*. Preparation, structure analysis and photoluminescence properties of $MgGa_2O_4:Mn^{2+}$. *Opt Mater* 2009, **31**: 1620–1627.

[12] Luchechko A, Zhydachevskyy Y, Maraba D, *et al*. TL and OSL properties of Mn^{2+}-doped $MgGa_2O_4$ phosphor. *Opt Mater* 2018, **78**: 502–507.

[13] Ahn W, Im M, Kim YJ. Effects of flux on the luminescence of $MgGa_2O_4:Mn^{2+}$ phosphors. *Mater Res Bull* 2017, **96**: 254–257.

[14] Kravets O, Zaremba O, Shpotyuk Y, *et al*. Structure, morphology and optical-luminescence investigations of spinel $ZnGa_2O_4$ ceramics co-doped with Mn^{2+} and Eu^{3+} ions. *Appl Nanosci* 2019, **9**: 907–915.

[15] Zhang Y, Wu ZJ, Geng DL, *et al*. Full color emission in $ZnGa_2O_4$: Simultaneous control of the spherical morphology, luminescent, and electric properties via hydrothermal approach. *Adv Funct Mater* 2014, **24**: 6581–6593.

[16] Kansy J. Microcomputer program for analysis of positron annihilation lifetime spectra. *Nucl Instrum Meth Phys Res Sect A: Accel Spectrometers Detect Assoc Equip* 1996, **374**: 235–244.

[17] Krause-Rehberg R, Leipner HS. *Positron Annihilation in Semiconductors*. Berlin, Heidelberg: Springer Berlin Heidelberg, 1999.

[18] Tuomisto F, Makkonen I. Defect identification in semiconductors with positron annihilation: Experiment and theory. *Rev Mod Phys* 2013, **85**: 1583–1631.

[19] Saarinen K, Hautojärvi P, Corbel C. Chapter 5 positron annihilation spectroscopy of defects in semiconductors. *Semiconduct Semimet* 1998, **51**: 209–285.

[20] Jean YC, Mallon PE, Schrader DM. Introduction to positron and positronium chemistry. In *Principles and Application of Positron and Positronium Chemistry*. New Jersy: World Scientific, 2003: 1–15.

[21] Li YX, Niu PJ, Hu L, *et al*. Monochromatic blue-green and red emission of rare-earth ions in $MgGa_2O_4$ spinel. *J Lumin* 2009, **129**: 1204–1206.

[22] Sawada K, Nakamura T, Adachi S. Europium gallium garnet ($Eu_3Ga_5O_{12}$) and Eu_3GaO_6: Synthesis and material properties. *J Appl Phys* 2016, **120**: 143102.

[23] Shpotyuk O, Ingram A, Klym H, *et al*. PAL spectroscopy in application to humidity-sensitive $MgAl_2O_4$ ceramics. *J Eur Ceram Soc* 2005, **25**: 2981–2984.

[24] Vijay YK, Wate S, Awasthi DK, *et al.* Ion induced effects in polymers. *Indian J Eng Mater S* 2000, **7**: 375–377.

[25] Shpotyuk O, Filipecki J, Ingram A, *et al*. Positronics of subnanometer atomistic imperfections in solids as a high-informative structure characterization tool. *Nanoscale Res Lett* 2015, **10**: 77.

[26] Shpotyuk O, Ingram A, Shpotyuk Y. Free-volume characterization of nanostructurized substances by positron annihilation lifetime spectroscopy. *Nucl Instrum Meth Phys Res Sect B: Beam Interactions Mater Atoms* 2018, **416**: 102–109.

[27] Mironova N, Skvortsova V, Smirnovs A, *et al*. Distribution

of manganese ions in magnesium-aluminium spinels of different stoichiometries. *Opt Mater* 1996, **6**: 225–232.

[28] Judd BR. Optical absorption intensities of rare-earth ions. *Phys Rev* 1962, **127**: 750.

[29] Ofelt GS. Intensities of crystal spectra of rare-earth ions. *J Chem Phys* 1962, **37**: 511–520.